Energy Absorption during Projectile Perforation of Thin Steel Plates and the Kinetic Energy of Ejected Fragments

J. Dean, C.S. Dunleavy, P.M. Brown, T.W. Clyne

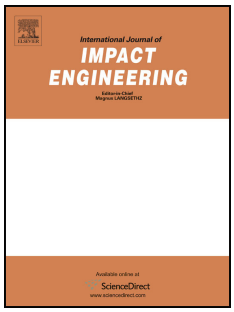

Title: Energy Absorption during Projectile Perforation of Thin Steel Plates and the Kinetic Energy of Ejected Fragments

Authors: J. Dean, C.S. Dunleavy, P.M. Brown, T.W. Clyne

PII: S0734-743X(09)00090-6

DOI: 10.1016/j.ijimpeng.2009.05.002

Reference: IE 1777

To appear in: *International Journal of Impact Engineering*

Received Date: 21 August 2008

Revised Date: 2 May 2009

Accepted Date: 10 May 2009

Please cite this article as: Dean J, Dunleavy CS, Brown PM, Clyne TW. Energy Absorption during Projectile Perforation of Thin Steel Plates and the Kinetic Energy of Ejected Fragments, International Journal of Impact Engineering (2009), doi: 10.1016/j.ijimpeng.2009.05.002

re-submitted to Int. J. Impact Eng., May 2009

Energy Absorption during Projectile Perforation of Thin Steel Plates and the Kinetic Energy of Ejected Fragments

J. Dean[1], C. S. Dunleavy[1], P. M. Brown[2] & T. W. Clyne[1]

[1] Department of Materials Science & Metallurgy
Cambridge University
Pembroke Street, Cambridge CB2 3QZ, UK

[2] DSTL
Physical Sciences Research Department
Salisbury, UK

Abstract

This paper concerns energy absorption in thin (0.4 mm) steel plates during perforation by spherical projectiles of hardened steel, at impact velocities between 200 and 600 m s^{-1}. Absorbed energies have been obtained from measured incident and emergent projectile velocities. These tests were simulated using ABAQUS/Explicit, using the Johnson and Cook plasticity model. A-strain rate-dependent, critical plastic strain fracture criterion was employed to model fracture. Good agreement is obtained between simulations and experiment and the model successfully captures the transitions in failure mode as projectile velocity increases. At velocities close to the ballistic limit, the plates fail by dishing and discing. As the incident velocity is increased, there are two transitions in failure mode, firstly to shear plugging and secondly to fragmentation and petalling. The simulations also show that, during the latter mode of failure, the kinetic energy of ejected debris is significant, and failure to include this contribution in the energy balance leads to a substantial over-estimate of the energy absorbed within the sheet. Information is also presented relating to the strain rates at which plastic deformation occurs within the sample under different conditions. These range up to about 10^5 s^{-1}, with the corresponding strain rate hardening effect being quite substantial (factor of 2-3 increase in stress).

Keywords; Ballistic; Impact; Perforation; ABAQUS; Johnson & Cook; 304 stainless steel.

1 Introduction

Perforation of plates during projectile impact is a complex process, commonly involving elastic and plastic deformation, strain and strain rate hardening effects, thermal softening, crack formation, adiabatic shearing, plugging, petalling and even shattering. These effects depend on the properties and geometries of projectile and target and on the incident velocity. There have been many theoretical and experimental studies in this area, which are covered in the comprehensive reviews of Corran et al [1], Anderson and Bodner [2] and Corbett et al [3]. Specific studies have been undertaken on petalling phenomena [4, 5], shear plugging failure [6, 7] and dishing [8] in thin metallic plates, while the effects of target thickness, impact obliquity [9] and projectile nose shape [10, 11] have also been studied.

The main failure modes are ductile hole enlargement (lateral displacement of material), petal formation, plugging failure via through-thickness shear (often accompanied or preceded by adiabatic heating), dishing, which is characterised by large plate deflection, membrane stretching and tensile tearing (discing) and, finally, fragmentation. It is not uncommon for a combination of these failure modes to operate simultaneously. Furthermore, the failure mode often changes with increasing projectile velocity [12].

The Finite Element Method (FEM) has become an increasingly useful tool for the analysis of impact events, and current commercial codes are well suited to dealing with problems involving large deformations and elevated strain rates. The necessary computational resources are also routinely available. However, as highlighted by Zukas [13], erroneous results can be obtained. Common errors include the use of models that are ill-suited to the problem, failure to recognise numerical instabilities (which may be attributed to physical phenomena), poor mesh specification, and use of inappropriate property data and constitutive relations. Of these, the latter are amongst the most common and, potentially, most significant.

The constitutive behaviour of most metals is, in general, fairly well understood and standard expressions are routinely implemented into FEM codes. These normally incorporate the effects of strain, strain rate and temperature on the effective stress. Examples include the phenomenological model of Johnson & Cook [14] and the more theoretical, dislocation dynamics-based models of

Zerilli and Armstrong [15]. The Johnson & Cook plasticity model is well suited to high rate deformation, and in general is reported to capture the main features of penetration and perforation – an example being the studies of Borvik et al [7, 16, 17] on projectile penetration of steel and aluminium sheets. Their simulations agree reasonably well with experimental data, particularly at high velocities, with high mesh densities and when using an adaptive re-meshing algorithm. Gupta et al [10] also used a Johnson & Cook elastic-viscoplastic model, to simulate penetration experiments on 1 mm thick Al sheets. Their model included the effects of linear thermo-elasticity, yielding, plastic flow, isotropic strain hardening, strain rate hardening and softening due to adiabatic heating. They successfully predicted the residual velocities of penetrating projectiles, as well as ballistic limit velocities.

Simulations of this type commonly employ fracture criteria. These can be either instantaneous, time-dependent or micromechanical [13]. Micromechanical models are often preferred, despite their complexity, since they are usually more reliable [13]. In a comparative study of six fracture conditions, including a simple critical fracture strain, Teng and Wierzbicki [18] found that those based on accumulated equivalent plastic strain were most reliable. One such fracture criterion is that of Johnson & Cook, which has been widely employed [10, 16, 17, 19] for simulating the perforation of metallic plates. It can be expressed in the form

$$\bar{\varepsilon}_{f,pl} = \left[D_1 + D_2 \exp\left(D_3 \sigma^*\right)\right]\left[1 + D_4 \ln\left(\frac{\left(\mathrm{d}\bar{\varepsilon} / \mathrm{d}t\right)_{pl}}{\left(\mathrm{d}\varepsilon / \mathrm{d}t\right)_0} \right)\right]\left(1 + D_5\theta\right) \qquad (1)$$

(A nomenclature listing is included in this paper as an Appendix.) However, whilst the Johnson & Cook plasticity parameters are relatively easy to determine from simple mechanical tests (at least for low strain rates), the fracture constants (D_1…..D_5) are more difficult to obtain. Multiple tests must be conducted over a wide range of strain rate and stress triaxiality. In the current study, a strain rate-dependent, critical plastic strain criterion is employed, which requires relatively few parameters to be evaluated. This fracture criterion was coupled with the Johnson and Cook plasticity model (§ 3.2.2).

A further potential complication at high strain rates is the possible formation of adiabatic shear bands. These are bands of localised plastic shear strain, within which large temperature rises can

occur. If the associated thermal softening exceeds the strain hardening, then continued loading is likely to result in failure at stress levels well below the static strength of the material at ambient temperature [20, 21]. Adiabatic shear band formation has been modelled numerically [7, 22, 23]. For example, Chou et al [23] showed, using Johnson & Cook constitutive relations, that shear bands are commonly expected if thermal softening is taken into account. They noted, however, that a relatively fine mesh size is often required in order to capture their formation. In steels, for example, they are typically 10-100 μm in width, so local mesh dimensions need to be correspondingly fine.

The experimental work in the present study concerns 304 stainless steel. To the authors' best knowledge, the only previous study on this material, over the impact velocity range covered here, is that of Yungwirth et al [24], who examined the ballistic performance of sandwich panels with pyramidal lattice cores and compared it with that of monolithic plate of equal areal density. As impact velocities were increased beyond the ballistic limit, they observed a small decrease in the specific absorbed energy by the monolithic plates, followed by a monotonic increase.

2 Experimental Procedures

Tensile test specimens were cut using Electric Discharge Machining (EDM), from 0.4 mm thick sheets of grade-304 stainless steel that had been annealed in inert atmosphere at a temperature of 1195°C for 1.5 hours. Tensile tests were conducted using a 10 kN ESH servo-hydraulic testing machine at a strain rate of 0.01 s^{-1}. Strain was measured using a linear variable displacement transducer (LVDT). Stress-strain responses were recorded and material property data were inferred.

Circular disk specimens were cut, using EDM, from the stainless steel sheets. Specimens, of 76.5 mm diameter, were rigidly clamped around the periphery, such that a circle of 60 mm diameter was exposed. Specimens were impacted at normal incidence, with a range of incident velocities, by spherical projectiles of hardened steel, 8 mm in diameter and of 2 g mass. At low projectile velocities (170-250 m s^{-1}), the incident velocity was measured using a series of light gates, comprising three light emitting diodes and three light receiving photodiodes. The residual

velocity was measured using an electromagnetic induction technique, based on measurement of the delay between the generation of current in two copper coils, separated by a known distance, when the moving (magnetic) projectile passes through them. At intermediate projectile velocities (~250-350 m s^{-1}), incident and residual velocities were measured using high speed video equipment (Photo-sonics Phantom V4.3 high speed video camera). The inter-frame and exposure times were in the ranges 10-36 μs and 6-9 μs. The projectile velocity was calculated from the inter-frame time and the distance travelled, using the Photo-sonics Phantom software. At high projectile velocities (~350-600 m s^{-1}), a high speed framing camera was employed (since a shorter exposure time was required). The high speed photographic images were taken with an Ultranac FS501 image converter camera, capturing 12 sequential images on Polaroid film. The projectiles were back-illuminated, using a Bowens flash (with a light duration of several ms). The exposure time for all of the images was 1 μs and the inter-frame times ranged from 10-70 μs. Over the critical period (~170 μs), 12 polaroid images were captured. After penetration, impacted specimens were sectioned using EDM and photographed. Specimens were weighed before and after testing, and mass losses (due to the ejection of plugs or multiple fragments) were calculated.

3 Numerical Modelling

3.1 Mesh Formulation and Boundary Conditions

The steel sheets were modelled as elastic-plastic shells and meshed with reduced integration, linear quadrilateral shell elements – type S4R. The shell element formulation is well suited to dynamic analyses involving large plastic bending strains [25]. The mesh density was refined in the region directly beneath the impact site. The sensitivity of the predicted results to mesh density was a key concern during the simulations (particularly since large strain gradients were expected), and there exists a threshold mesh density value for solution convergence. Table III shows the predicted absorbed energy as a function of mesh density and minimum element size for an impact velocity of 600 m/s, which is insensitive to further refinements beyond 2457 elements.

An encastré boundary condition was specified to simulate the clamping conditions. The projectile was modelled as an analytical rigid body and simply assigned mass. This assumes that

projectile deformation is negligible and observations of projectiles after impact confirmed that there was no noticeable plastic deformation. Penalty contact was defined between the projectile and the plate. Friction between the projectile and the plate was taken as negligible, which is consistent with the results of Krafft [26], who showed experimentally that sliding friction typically absorbs less than 3% of the total incident energy.

3.2 Material Response Characterisation

3.2.1 Johnson & Cook Plasticity

The Johnson & Cook plasticity formulation, which defines the flow stress as a function of equivalent plastic strain, strain rate and temperature, was employed in all simulations The dynamic flow stress is expressed by the following relation [14]

$$\bar{\sigma}_d = \left[A + B(\bar{\varepsilon}_{pl})^n \right] \left[1 + C \ln \left(\frac{\left(\mathrm{d}\bar{\varepsilon} / \mathrm{d}t \right)_{pl}}{\left(\mathrm{d}\varepsilon / \mathrm{d}t \right)_0} \right) \right] (1 - \theta) \tag{3}$$

where σ_d is the dynamic flow stress, $\bar{\varepsilon}_{pl}$ is the equivalent plastic strain, $\left(\mathrm{d}\bar{\varepsilon} / \mathrm{d}t \right)_{pl}$ is the equivalent plastic strain rate, $\left(\mathrm{d}\varepsilon / \mathrm{d}t \right)_0$ is a reference strain rate, *A*, *B*, *n*, *m* and *C* are material parameters and θ is the non-dimensional temperature given by:

$$\hat{\theta} \equiv \begin{cases} 0 & \theta < \theta_{\text{transition}} \\ \left(\theta - \theta_{transition} \right) / \left(\theta_{melt} - \theta_{transition} \right) & \theta_{\text{transition}} \le \theta \le \theta_{melt} \\ 1 & \theta > \theta_{melt} \end{cases} \tag{4}$$

where θ is the current temperature, θ_{melt} is the melting temperature and $\theta_{transition}$ is the transition temperature defined as the one at or below which there is no temperature dependence on the expression of the yield stress. The constant *A* is the yield stress under quasi-static conditions, *B* and *n* are strain hardening parameters, *m* controls the temperature dependence and *C* the strain rate dependence. The values of the Johnson & Cook parameters used in the present work, which were obtained from Lee et al [27], are listed in Table I, and the data are plotted in Fig.1. This does, of course, assume that the material used in this study is similar to that of Lee et al [27]. This isn't entirely satisfactory, since microstructural differences could affect the mechanical properties.

However, since these data [27] are reportedly [28] representative of annealed 304 stainless steel, it seems likely that they are at least broadly appropriate for the present work.

3.2.3 Fracture

A strain rate–dependent, critical plastic strain-based fracture criterion was employed. The equivalent plastic strain at the onset of fracture $\bar{\varepsilon}_{D.pl}$ is assumed to be a function of the equivalent plastic strain rate and stress triaxiality, ie $\bar{\varepsilon}_{D,pl}\left(\left(\mathrm{d}\bar{\varepsilon}/\mathrm{d}t\right)_{pl},\Sigma\right)$. The stress triaxiality is the ratio of the mean stress to the equivalent stress, and thus characterises the degree to which plasticity is being promoted, which is known to affect the likelihood of fracture – as the triaxiality increases, the strain to fracture decreases [29]. The base level (maximum) triaxiality can be calculated using Bridgman's analysis [30], from the initial notch diameter, although to determine this parameter over a range of strain rate and temperature requires a significant number of tests [31].

In any case, it has previously been reported that [29] Bridgman's theory can lead to inaccurate estimates of the stress triaxiality, and no such tests were conducted during the current work. Instead, a triaxiality of 1/3 was assumed, based on the work of Zhou [32]. This is a plausible approximation, assuming that the plate material can be treated as a shell, with plane stress conditions satisfied. A stress triaxiality of 1/3 does, however, imply that the stress state of the plate is dominated by uniaxial tension, which is not strictly true. It is also worth noting that, in the parametric study conducted by Borvik et al [29], the stress triaxiality was nearly insensitive to strain rate and inertia. The stress triaxiality was also relatively insensitive to temperature.

The damage, once initiated, is assumed to evolve linearly until the material is fully degraded and can no longer sustain load. The damage, D, accumulates in an element according to the following relation:

$$D = \sum \frac{\Delta\bar{\varepsilon}_{pl}}{\varepsilon_{f.pl}} \tag{5}$$

where $\Delta\bar{\varepsilon}_{pl}$ is the increment of accumulated equivalent plastic strain and $\varepsilon_{f,pl}$ is the plastic strain to failure. Failure occurs when $D \geq 1$; once this condition is satisfied in an element, it is removed from the mesh. The fracture strain is established as a tabular function of strain rate. However, since high strain rate fracture data were unavailable, and following the work of Lichtenfeld et al

[33] on type-304 stainless steel, the fracture strain was assumed to decrease by 20% (compared to the quasi-static value – measured experimentally) for a strain rate of 10^4 s^{-1}. A progressive reduction in fracture strain was assumed over the strain rate range, as shown in Fig.1.

3.2.5 Extraction of Global Information about Strain Rate Distributions

For each volume element, during each time interval, the average strain rate at which deformation occurred was recorded, as was the strain induced and the plastic work done. These increments of energy were accumulated into a series of bins covering specific strain rate ranges. For cases in which the strain rate varied during the time interval beyond the range covered by a single bin, the energy was partitioned between the bins concerned using a proportional algorithm. This algorithm is relatively crude, but it was ensured that the time interval of the computations was short enough to ensure that the associated error was small. (As with other aspects of the computation, it was confirmed that the meshing and time interval selection were sufficiently refined to ensure that they had no significant effect on the predictions.)

A "characteristic strain rate", representing the mean strain rate throughout the specimen for a given incident velocity, was calculated by considering all volume elements, across the complete time domain, weighted by the fraction of energy absorbed in a given element during a given time step. It was obtained by simply multiplying each strain rate bin upper boundary by the corresponding fraction of energy absorbed within that strain rate bin. A summation was then made for all bins.

4 Model Predictions and Comparisons with Experimental Data

4.1 Effects of Projectile Incident Velocity

A summary is shown in Table II of the experimental data obtained from each run. The table includes incident and residual projectile velocities, corresponding loss of projectile kinetic energy (ΔU), loss of specimen mass after impact, associated fragment kinetic energy (obtained assuming that all fragments acquire the residual projectile velocity) and the energy absorbed within the specimen (difference between energy loss of projectile and kinetic energy of fragments). A comparison is shown in Fig.2(a) between experimental data and predictions, obtained using the

Johnson and Cook plasticity formulation, for the residual velocity as a function of the incident velocity. It can be seen that the level of agreement is very good.

The main focus of the present study is on the energy absorbed by the plate, and the associated deformation and fracture mechanisms. The energy absorbed in the plate is expected to be (predominantly) dissipated via plastic deformation and fracture, i.e. bulging, dishing, discing, petalling, plugging or fragmentation. For an individual element, the energy dissipated is given by:

$$U_{element} = \int_0^{\varepsilon \le \varepsilon_f} \sigma\left(\varepsilon, \left(\mathrm{d}\bar{\varepsilon} / \mathrm{d}t\right), T\right) \mathrm{d}\varepsilon \qquad (6)$$

so that the total work done is equal to

$$U_{plate} = \sum_1^n U_{element} \qquad (7)$$

Fig.2(b) shows the experimental data of Fig.2(a), re-plotted as absorbed energies (difference between incident and emergent projectile kinetic energies). It can be seen that agreement with experiment is good over the complete range of (sub-sonic) incident velocities being investigated here. Also plotted in Fig.2(b) is the predicted energy absorbed within the specimen by plastic deformation and fracture – i.e. excluding the kinetic energy associated with expelled fragments (Eq.6). It can be seen that, as expected, this contribution to the absorbed energy becomes significant at higher incident velocities (>~300 m s^{-1}), such that fragment expulsion starts to become significant. At an incident velocity of the order of 600 m s^{-1}, it constitutes over 50% of the total energy absorbed, although admittedly this energy now represents just a small fraction of the kinetic energy of the incident projectile.

The failure modes observed during these experiments are: (i) dishing and discing, (ii) shear plugging, and (iii) fragmentation. Fig.3 shows the predicted deformation histories for impact speeds of 200, 316 and 580 m s^{-1}. Fig.4 shows the experimental and predicted specimen shapes after projectile penetration. It can be seen that there is excellent agreement in terms of specimen appearance, and the transitions in failure mode with incident velocity are accurately predicted. Dishing and discing-type failures occur at low velocities, just above the ballistic limit (~160 m s^{-1}), with associated bulging, deflection and membrane stretching (tensile tearing) of the

sheet. Plugging failure occurs at higher impact velocities (>~250 m s^{-1}), with little or no dishing (but with some petalling), characterised by the removal of a plug of material with a diameter similar to that of the projectile (often slightly smaller for thin plates). A sequence of high speed video images (Fig.5) show plug ejection, for an impact velocity of 316 m s^{-1}. At higher impact velocities (>~400 m s^{-1}), failure tends to occur by a combination of extensive petal formation and fragmentation.

4.2 Kinetic Energy of Ejected Plugs or Fragments

It is clear from the predictions shown in Fig.3(b) that, for incident velocities sufficient to create plugging or fragmentation failure, the kinetic energy associated with these fragments can constitute a significant proportion of the total energy absorbed by the specimen, and indeed represents over half of the total for very high incident velocities (~600 m s^{-1}). The high speed photograph shown in Fig.6 confirms that fragments can be seen emerging after penetration of the specimen and the mass loss data shown in Table II confirms that this is occurring. It's fairly clear that plug and fragment velocities can be in a similar range to the residual projectile velocity. Fig.7 shows predicted velocity histories for the projectile and for the plug which is ejected by it, for a case in which plugging occurs.

A comparison is presented in Fig.8 between model predictions and experimental data for the fragment kinetic energy, as a function of the incident projectile velocity. These experimental data were obtained from measured mass loss data (see Table II), so the agreement exhibited here constitutes evidence of the reliability of the model which is independent of the comparison shown in Fig.3(b). Of course, the assumption that all fragments acquire a velocity equal to the residual velocity of the projectile is a rather crude one, which is probably responsible for some of the scatter in the experimental data in Fig.8, but in general it is expected to be a fair approximation and this is consistent with the level of agreement between predicted and experimental data in Fig.8.

4.2 Deformation Mechanisms and Local Strain Rates

The predictions shown in Fig.3(b) indicate that the energy absorbed within the specimen (by plastic deformation, fracture etc), shows a tendency to reach a plateau as the projectile velocity is

increased. This is not unexpected, since the specimen volume within which plastic deformation occurs does not change much with increasing projectile velocity (indeed, it tends to fall, compared with the behaviour at low impact velocities – see below), and there is a limit to the levels of plastic strain which can be generated within this volume.

It is of interest to consider the strain rates experienced by different regions while deformation takes place. Fig.9 shows, for three increasing projectile velocities, the proportion of the plastic work absorbed within the specimen, as a function of the strain rate at which this plastic deformation occurred. Naturally, the strain rates at which most of the deformation takes place tend to rise as the projectile velocity is increased.

However, some interesting effects can be identified on examining these data more closely. For example, Fig.10(a) shows the predicted dependence on projectile velocity of the characteristic (mean) strain rate within a specimen (see §3.2.5). It can be seen that, while there is a trend for this strain rate to increase as the incident velocity goes up, there is actually a dip over the range of 300-400 m s^{-1}. This is the approximate range over which plugging occurs – see Fig.8. It's certainly plausible that the onset of this failure mechanism should lead to a reduction in the average strain rate, since deformation rates will tend to be relatively low within a plug being pushed by a projectile, while straining in neighbouring material will also tend to be curtailed at a relatively early stage as the plug becomes detached. These changes in mechanism are also reflected in the curve shown in Fig.10 (b), which shows how the volume of material subjected to plastic deformation changes as the projectile velocity increases. It can be seen that this has a peak value at the ballistic limit, falls off as the velocity increases within the regime of dishing and discing (and the dishing becomes more localised), remains low while plugging failure occurs and rises slightly as fragmentation replaces plugging.

It's also of interest to note the absolute values of typical strain rates created during this kind of deformation. It can be seen in Fig.9 that these range up to about 3 10^4 s^{-1}, for a projectile velocity of 200 m s^{-1}, and up to about 3 10^5 s^{-1}, for a velocity of 600 m s^{-1}. Naturally, these strain rate values will tend to vary with projectile size and sheet thickness (and also with sheet material), but these calculations certainly give an indication of the nature of the deformation taking place within

the specimen under this type of loading. It's of interest to note (Fig.1) that, according to the Johnson-Cook formulation for this material, strain rates of ~10^5 s^{-1} generate stress level enhancements (compared to the quasi-static case) by factors of at least about 2 - i.e. substantial strain rate hardening occurs under these experimental conditions.

Of course, it must be borne in mind that these predictions would themselves be affected if a different strain rate sensitivity were to be incorporated into the constitutive equations employed. There's no doubt that it is preferable to use experimental stress-strain data obtained over a wide range of imposed strain rate, although obtaining these data can be time-consuming and difficult. In fact, due to the lack of literature data relating to strain rates above 10^4 s^{-1}, the constitutive relation for that strain rate (see Fig.1) was employed in the present work for all higher strain rates as well, which is clearly not really appropriate or satisfactory. Nevertheless, the FEM predictions presented here do appear to capture most of the main features of the response of this particular material to this type of ballistic loading. In order to investigate further and more deeply, it would be advisable to bring the micro-mechanisms of deformation clearly into the picture, rather than simply trying to identify the most reliable constitutive relations without reference to the effects responsible for them.

5 Conclusions

The following conclusions can be drawn from this work.

(a) Thin (0.4 mm) plates of 304 stainless steel were perforated by spherical steel projectiles, with a range of (sub-sonic) incident velocities (up to 600 m s^{-1}). Absorbed energies were obtained experimentally from incident and emergent projectile velocities. The tests were simulated using the Explicit FEM code in ABAQUS/CAE. The Johnson and Cook plasticity algorithm was employed. This was coupled with a strain rate-dependent, critical plastic strain fracture criterion.

(b) The predicted amount of energy absorbed by the specimen was found to agree well with the experimental data over the complete range of projectile velocity. The model also captured the transitions in failure mode, from dishing at low velocities, to plugging failure at around 300-400 m s^{-1} and a fragmentation process at higher velocities. It is shown that, towards the upper end of the velocity range investigated, the contribution to the total energy absorbed represented by the kinetic energy of escaping small fragments of the specimen becomes highly significant (>50% of the total).

(c) A study has been made of the strain rates at which the deformation takes place within specimens of this type, during ballistic impact. While, in general, there is a tendency for strain rates to increase at higher impact velocities, it has been shown that the failure mode is important. For example, the sequence of events during plugging failure is such that the mean strain rate tends to fall somewhat as the velocity becomes high enough for it to become dominant. The strain rates that are operative while most of the plastic deformation occurs during ballistic impact fall mostly in the range of 10^2 – 10^4 s^{-1} for an incident velocity of 200 m s^{-1} and 10^3 – 10^5 s^{-1} for an incident velocity of 600 m s^{-1}. At strain rates of this magnitude, this steel exhibits substantial strain rate hardening and it's clearly important to have reliable input data concerning this effect if these impact processes are to be realistically modelled. There is currently a shortage of such data for most materials.

Acknowledgements

Financial support has come from DSTL (for JD), and from EPSRC (for CSD). The DSTL contract number under which part of the work was done is RD033-3169. The authors are grateful for useful discussions with a number of researchers with an interest in this area, including Richard Jones (DSTL) and Andrew Wallwork, Giles Aldrich-Smith and Neil Bourne (AWE).

References

1. Corran, R.S.J., P.J. Shadbolt, and C. Ruiz, *Impact Loading of Plates - An Experimental Investigation.* International Journal of Impact Engineering, 1983. **1**(1): p. 3-22.
2. Anderson, C.E. and S.R. Bodner, *Ballistic Impact: The Status of Analytical and Numerical Modelling.* International Journal of Impact Engineering, 1988. **7**(1): p. 9-35.
3. Corbett, G.G., S.R. Reid, and W. Johnson, *Impact Loading of Plates and Shells by Free Flying Projectiles.* International Journal of Impact Engineering, 1996. **18**(2): p. 141-230.
4. Wierzbicki, T., *Petalling of Plates under Explosive and Impact Loading.* Int. J. Impact Eng., 1999. **22**: p. 935-954.
5. Landkof, B. and W. Goldsmith, *Petalling of Thin Metallic Plates During Penetration by Cylindro-Conical Projectiles.* International Journal of Solids and Structures, 1983. **21**(3): p. 245-266.
6. Atkins, A.G., M.A. Khan, and J.H. Liu, *Necking and Radial Cracking Around Perforations in Thin Sheets at Normal Incidence.* Int J Impact Eng, 1998. **21**(7): p. 521-539.
7. Borvik, T., O.S. Hopperstad, T. Berstad, and M. Langseth, *Numerical Simulation of Plugging Failure in Ballistic Penetration.* International Journal of Solids and Structures, 1999. **38**: p. 6241-6264.
8. Lee, Y.W. and T. Wierzbicki, *Fracture Prediction of Thin Plates under Localised Impulsive Loading. Part 1: Dishing.* Int J Impact Eng, 2005. **31**: p. 1253-1276.
9. Goldsmith, W., *Non-Ideal Projectile Impact on Targets.* International Journal of Impact Engineering, 1999. **22**(2-3): p. 95-395.
10. Gupta, N.K., M.A. Iqbal, and G.S. Sekhon, *Experimental and Numerical Studies on the Behaviour of Thin Aluminium Plates Subjected to Impact by Blunt- and Hemispherical-Nosed Projectiles.* International Journal of Impact Engineering, 2006. **32**: p. 1921 - 1944.
11. Borvik, T., M. Langseth, O.S. Hopperstad, and K.A. Malo, *Perforation of 12mm Thick Steel Plates by 20mm Diameter Projectiles with Flat, Hemispherical and Conical Noses, Part 1: Experimental Study.* Int J Impact Eng, 2002. **27**: p. 19 - 35.
12. Teng, X. and T. Wierzbicki, *Transition of Failure Modes in Round-Nosed Mass-to-Beam Impact.* Eur. J. Mech. A/Solids, 2008.
13. Zukas, J.A., *Some Common Problems in the Numerical Modeling of Impact Phenomena.* Computing Systems in Engineering, 1993. **4**(1): p. 43-58.
14. Johnson, G.R. and W.H. Cook, *Fracture Characteristics of Three Metals Subjected to Various Strains, Strain Rates, Temperatures and Pressures.* Engineering Fracture Mechanics, 1985. **21**(1): p. 31 - 48.
15. Zerilli, F.J. and R.W. Armstrong, *Dislocation-Mechanics-Based Constitutive Relations for Material Dynamics Calculations.* Journal of Applied Physics, 1987. **61**: p. 1816-1825.
16. Borvik, T., H.A. Clausen, M. Eriksson, T. Berstad, O.S. Hopperstad, and M. Langseth, *Experimental and Numerical Study on the Perforation of AA6005-T6 Panels.* International Journal of Impact Engineering, 2005. **32**: p. 35-64.
17. Borvik, T., M. Langseth, O.S. Hopperstad, and A.K. Malo, *Ballistic Penetration of Steel Plates.* International Journal of Impact Engineering, 1999. **22**: p. 855 - 886.
18. Teng, X. and T. Wierzbicki, *Evaluation of Six Fracture Models in Hgh Velocity Perforation.* Engineering Fracture Mechanics, 2006. **73**: p. 1653-1678.
19. Borvik, T., O.S. Hopperstad, T. Berstad, and M. Langseth, *Perforation Of 12mm Thick Steel Plates By 20mm Diameter Projectiles With Flat, Hemispherical And Conical Noses Part 2: Numerical Simulations.* Int J Impact Eng, 2002. **27**: p. 37-64.
20. Wright, T.W., *The Physics and Mathematics of Adiabatic Shear Bands*. 2002: Cambridge University Press.
21. Bai, Y. and B. Dodd, *Adiabatic Shear Localization*. First ed. 1992, Oxford: Pergamon Press. 378.
22. Roessig, K.M. and J.J. Mason, *Adiabatic Shear Localisation in the Dynamic Punch Test, Part 2: Numerical Simulations.* International Journal of Plasticity, 1999. **15**(2): p. 263-283.
23. Chou, P.C., J. Hashemi, A. Chou, and H.C. Rogers, *Experimentation and Finite Element Simulation of Adiabatic Shear Bands in Controlled Penetration Impact.* International Journal of Impact Engineering, 1991. **11**: p. 305-321.

24. Yungwirth, C.J., H.N.G. Wadley, J.H. O'Connor, A.J. Zakraysek, and V.S. Deshpande, *Impact Response of Sandwich Panels with a Pyramidal Lattice Core.* International Journal of Impact Engineering, 2008. **35**: p. 920-936.
25. ABAQUS, *ABAQUS/Explicit User's Manuals, Version 6.6*. 2006.
26. Krafft, J.M., *Surface Friction in Ballistic Penetration.* Journal of Applied Physics, 1955. **26**(10): p. 1248-1253.
27. Lee, S.C., F. Barthelat, J.W. Hutchinson, and H.D. Espinosa, *Dynamic Failure of Metallic Pyramidal Truss Core Materials - Experiments and Modelling.* International Journal of Plasticity, 2006. **22**: p. 2118-2145.
28. Maloy, S.A., G.T. Gray III, C.M. Cadt, R.W. Rutherford, and R.S. Hixson, *The Influence of Explosive-Driven "Taylor Wave" Shock Pre-straining on the Structure/Property Behaviour of 304 Stainless Steel.* Metallurgical and Materials Transactions A - Physical Metallurgy and Materials Science, 2004. **35**(9): p. 2617-2624.
29. Borvik, T., O.S. Hopperstad, and T. Berstad, *On the Influence of Stress Triaxiality and Strain Rate on the Behaviour of a Structural Steel. Part 2. Numerical Study.* European Journal of Mechanics A/Solids, 2003. **22**: p. 15-32.
30. Hill, R., *The Mathematical Theory of Plasticity*. 1950, London: Oxford University Press.
31. Dey, S., T. Borvik, O.S. Hopperstad, and M. Langseth, *On the Influence of Fracture Criterion in Projectile Impact of Steel Plates.* Computational Mater. Sci., 2006. **38**: p. 176-191.
32. Zhou, D., *Impact Response of Lightweight Sandwich Panels*, in *Dept. of Engineering*. 2005, University of Cambridge: Cambridge.
33. Lichtenfeld, J.A., M.C. Mataya, and C.J. van-Tyne, *Effect of Strain Rate on Stress-Strain Behaviour of Alloy 309 and 304L Austenitic Stainless Steel.* Metallurgical and Materials Transactions A, 2006. **37A**: p. 147.
34. Radford, D.D., G.J. McShane, V.S. Deshpande, and N.A. Fleck, *The Response of Clamped Sandwich Plates with Metallic Foam Cores to Simulated Blast Loading.* International Journal of Solids and Structures, 2006. **43**: p. 2243-2259.

Appendix - Nomenclature

A	(Pa)	Johnson-Cook Material Parameter
B	(Pa)	Johnson-Cook Material Parameter
C	(-)	Johnson-Cook Material Parameter
c_p	(J kg^{-1} K^{-1})	Specific heat
$D_1 - D_5$	(-)	Johnson-Cook Fracture Constants
E	(Pa)	Young's Modulus
m	(-)	Johnson-Cook Material Parameter
n	(-)	Johnson-Cook Material Parameter
R	(-)	Yield Strength Ratio
T	(K)	Temperature
t	(s)	Time
U	(J)	Energy
V	(m s^{-1})	Velocity
v	(m^3)	Volume
α	(-)	Proportion of deformation work converted to heat
ε	(-)	Strain
$\bar{\varepsilon}$	(-)	Equivalent Strain
$\left(\mathrm{d}\bar{\varepsilon} / \mathrm{d}t\right)$	(s^{-1})	Equivalent Strain Rate
$\left(\mathrm{d}\varepsilon / \mathrm{d}t\right)_0$	(s^{-1})	Reference Strain Rate
ρ	(kg m^{-3})	Density
σ	(Pa)	Stress
σ_Y	(Pa)	Yield Stress
σ_{UTS}	(Pa)	Ultimate Tensile Strength
$\bar{\sigma}$	(Pa)	Effective Stress
Σ	(-)	Stress Triaxiality
θ	(-)	Dimensionless temperature

Tables

ρ (kg m^{-3})	E (GPa)	ε_f (-)	A (MPa)	B (MPa)	n (-)	m (-)
7800	200	0.33	310	1000	0.65	1
T_m (K)	T_t (K)	C (-)	$\left(d\varepsilon / dt\right)_0$ (-)	α (-)	c_p (J kg^{-1} K^{-1})	
1673	293	0.07	0.01	0.95	440	

Table I Johnson & Cook plasticity and thermal property parameters for 304 stainless steel [27]

Run	V_{in} (m s^{-1})	V_{res} (m s^{-1})	ΔU (J)	m_{frag} (g)	U_{frag} (J)	U_{plate} (J)	Failure Mode
2	176.3	109.9	19.0	0	0	19.0	Hinged Cap
3	179.2	121.8	17.3	0	0	17.3	4 Petals
4	181.2	112.9	20.1	0	0	20.1	Hinged Cap
5	184.5	121.3	19.3	0	0	19.3	Hinged Cap
6	190.3	127.5	19.9	0	0	19.9	Hinged Cap
7	214.73	178.5	14.2	0	0	14.2	6 Petals
8	217.9	172.4	17.7	0	0	17.7	7 Petals
9	220.7	172.9	18.8	0	0	18.8	4 Petals
10	222.3	187.5	14.3	0.098	1.71	12.5	Plugging
11	228	188.6	16.4	0	0	16.4	Hinged Cap
12	310	286.09	14.3	0.156	6.38	7.9	Plugging/Petalling
13	316	290.21	15.6	0.250	10.54	5.1	Plugging/Petalling
14	318	292.24	15.7	0.199	8.50	7.2	Plugging/Petalling
15	576.5	541.53	39.1	0.222	32.58	6.5	Petalling/Fragments
16	580	544.43	40.0	0.202	29.91	10.1	Petalling/Fragments
17	583	545.98	41.8	0.237	35.34	6.4	Petalling/Fragments
18	592	560.47	36.3	0.114	17.94	18.4	Petalling/Fragments

Table II Measured projectile velocities and mass losses, inferred energy changes and observed failure modes for individual runs.

No. Of Elements	Minimum Element Size (μm)	Absorbed Energy (J)
220	815	49.36
585	433	45.89
1452	132	43.43
2457	120	42.075
4516	83	41.913
5818	41	41.863
6602	32	41.822

Table III: Mesh sensitivity analysis showing the predicted absorbed energys for an impact speed of 600 m s^{-1}

Figure Captions

Fig.1 *Stress-strain relationships for 304 steel, based on the Johnson-Cook plasticity relation, using parametric values obtained by Radford et al [34]and fracture strain information given by Lichtenfeld [33].*

Fig.2 *Comparison between measured and predicted dependence on incident velocity of (a) residual velocity (and (b) absorbed energy, based on Johnson-Cook input data (with and without the kinetic energy of specimen fragments being included in the predicted plots).*

Fig.3 *Model predictions, for the impact velocities shown, of the progression of fracture and the surface stress field, viewed from the rear of the specimen, for the times shown (after initial projectile contact).*

Fig.4 *Comparison between the modelled (left) and experimentally-observed (right) appearance of specimens after projectile penetration, as a function of incident velocity, showing (a) dishing, (b) shear plugging and (c) fragmentation modes of failure.*

Fig.5 *A sequence of high speed video images, showing the ejection of a plug following plate perforation at an incident velocity of 316 m s^{-1}.*

Fig.6 *High speed photograph taken during projectile emergence, after penetrating the specimen with an incident velocity of 592 m s^{-1}, with several ejected fragments, as well as the projectile, visible in flight.*

Fig.7 *Predicted histories of projectile and plug velocity, for an impact velocity of 316 m s^{-1}.*

Fig.8 *Comparison between the model predictions for the aggregate kinetic energy of ejected (single or multiple) fragments and experimental data, obtained by measurement of the lost mass and based on the assumption that all fragments emerge with the same velocity as the projectile.*

Fig.9 *Predicted work of deformation distributions over the range of strain rate, showing how the proportion of the total work done within a specimen (subjected to impact by a projectile with a given velocity) occurs within a series of bins covering the strain rate range.*

Fig.10 *Predicted dependence on incident velocity of (a) characteristic (mean) strain rate within the specimen throughout the process and (b) volume of material within which plastic deformation occurred.*

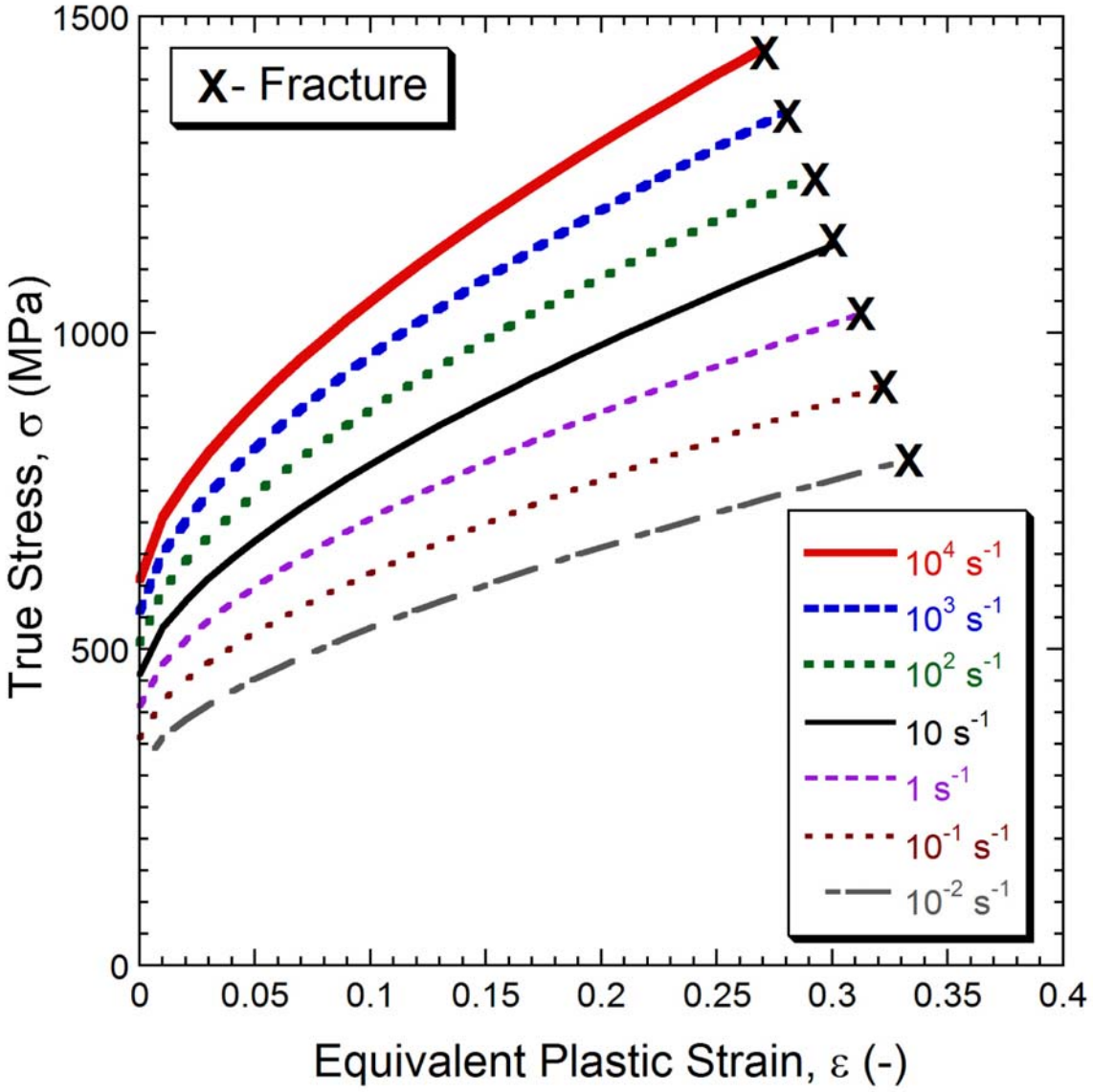
X- Fracture
True Stress, σ (MPa)
Equivalent Plastic Strain, ε (-)
0
500
1000
1500
0
0.05
0.1
0.15
0.2
0.25
0.3
0.35
0.4
10^4 s^-1
10^3 s^-1
10^2 s^-1
10 s^-1
1 s^-1
10^-1 s^-1
10^-2 s^-1

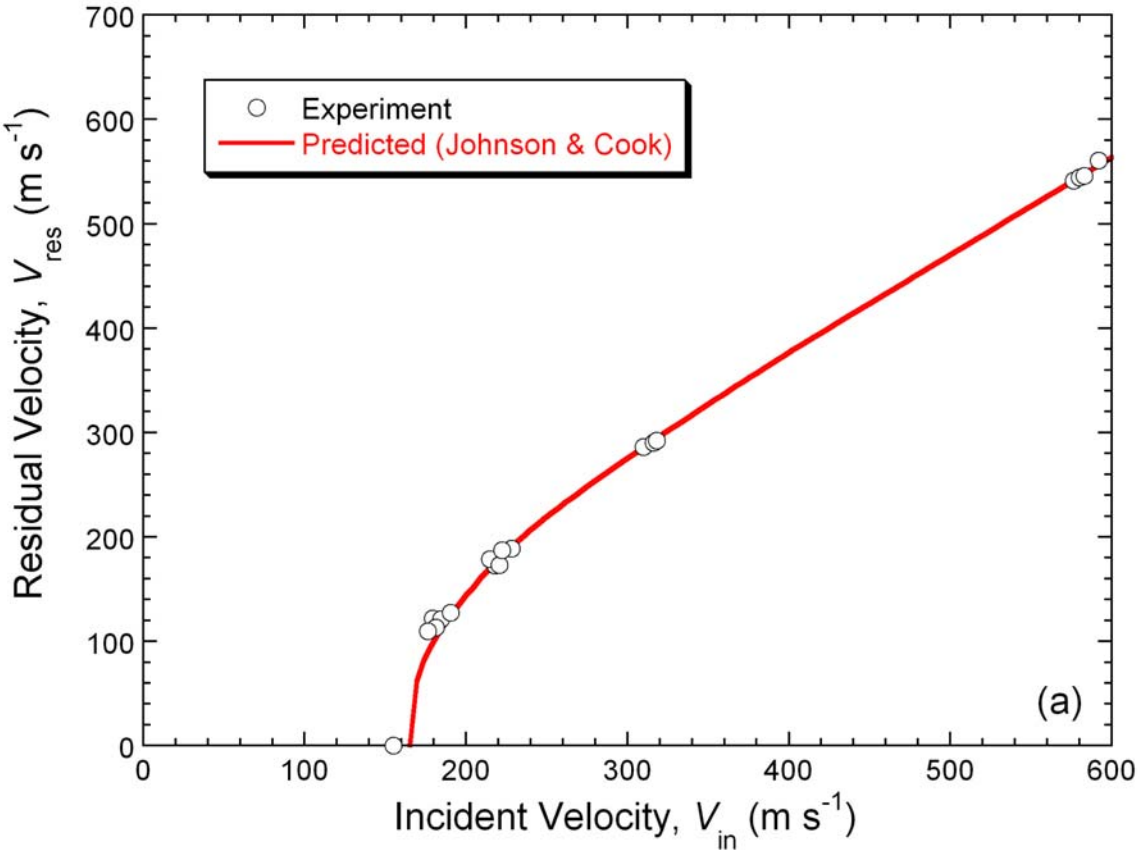
Experiment
Predicted (Johnson & Cook)
Residual Velocity, V_{res} (m s^{-1})
Incident Velocity, V_{in} (m s^{-1})
(a)
0
100
200
300
400
500
600
700

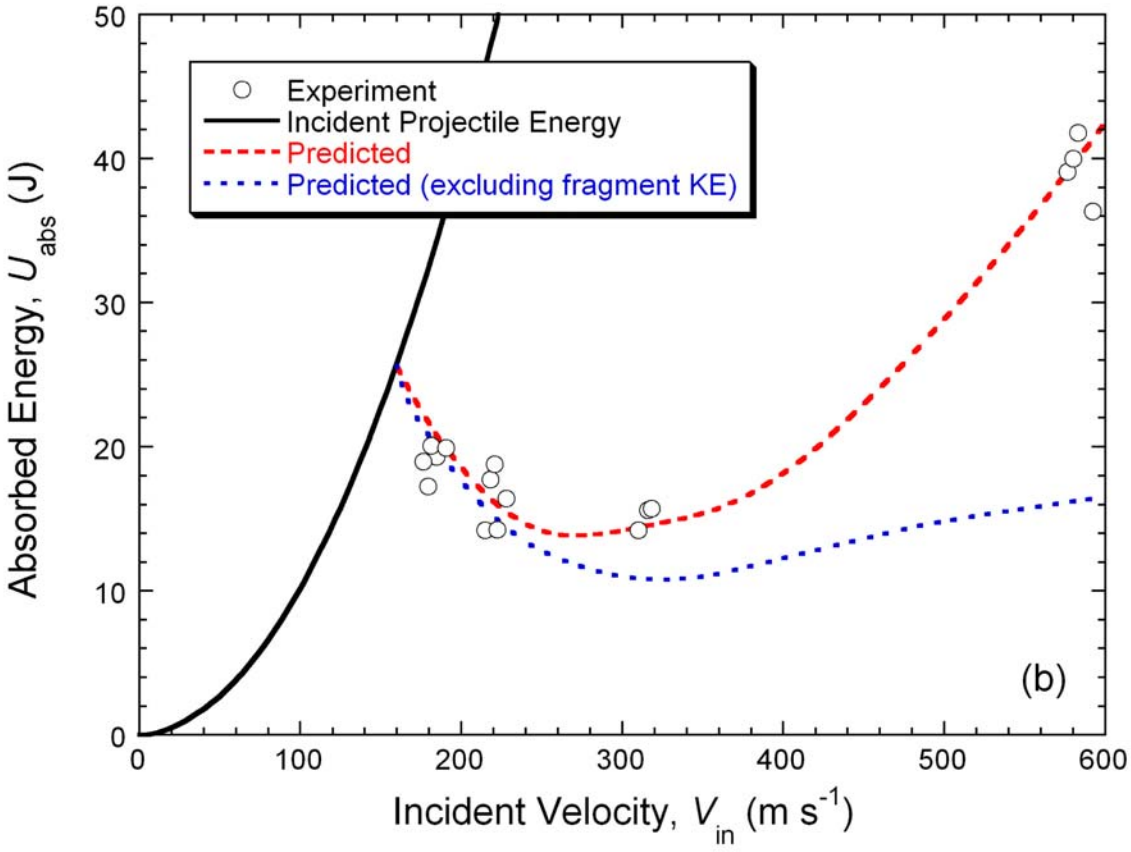
Experiment
Incident Projectile Energy
Predicted
Predicted (excluding fragment KE)
(b)
Absorbed Energy, U_{abs} (J)
Incident Velocity, V_{in} (m s^{-1})
0
10
20
30
40
50
0
100
200
300
400
500
600

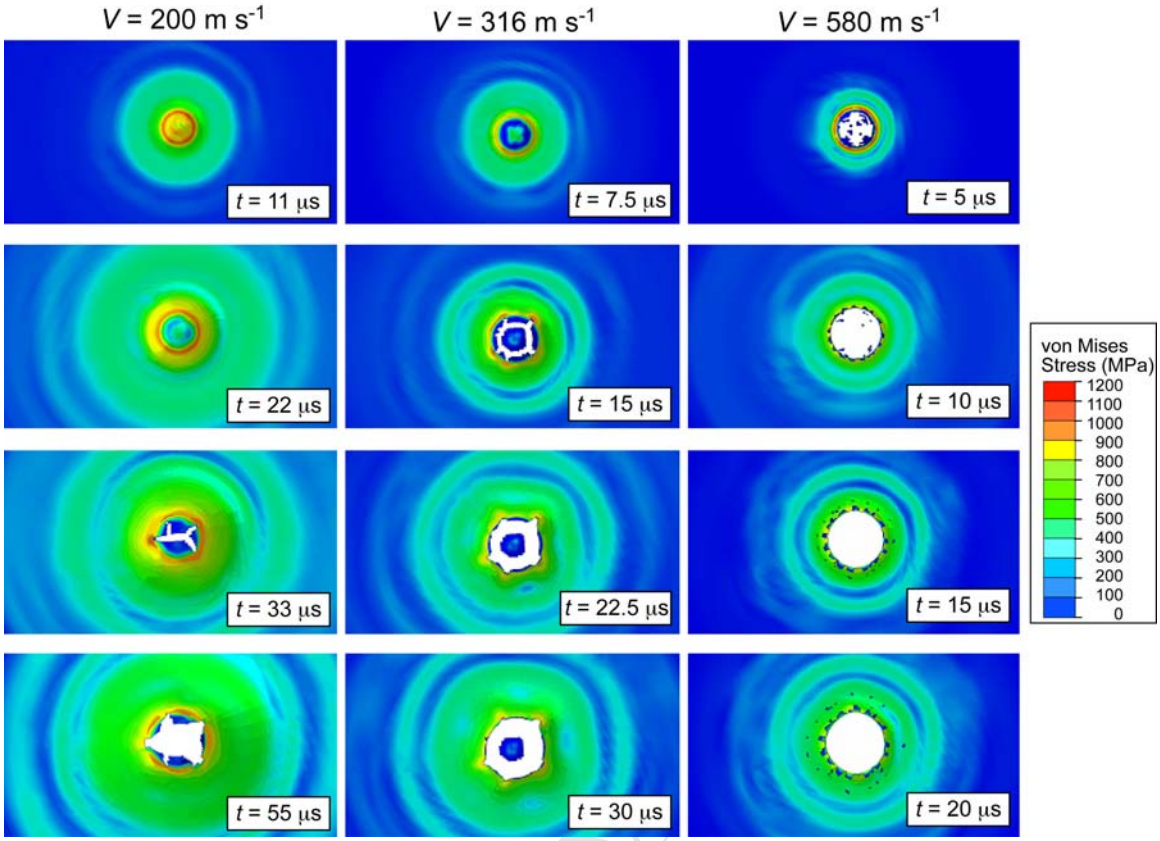

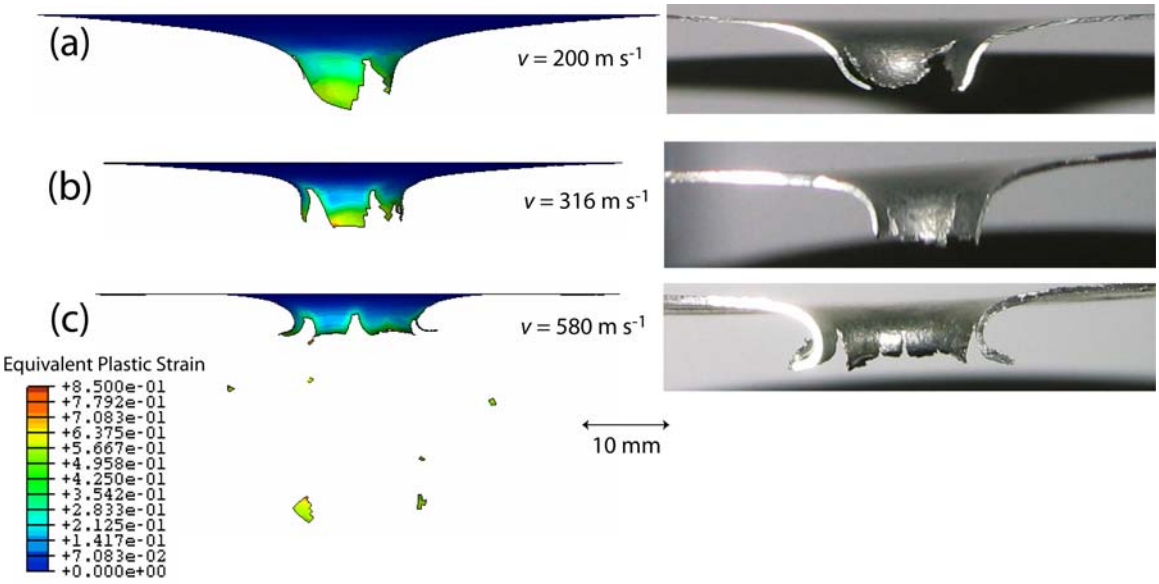

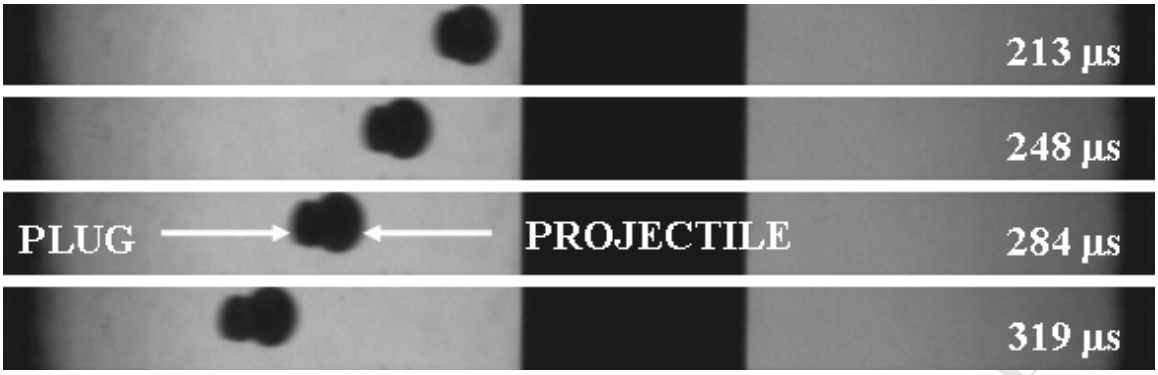

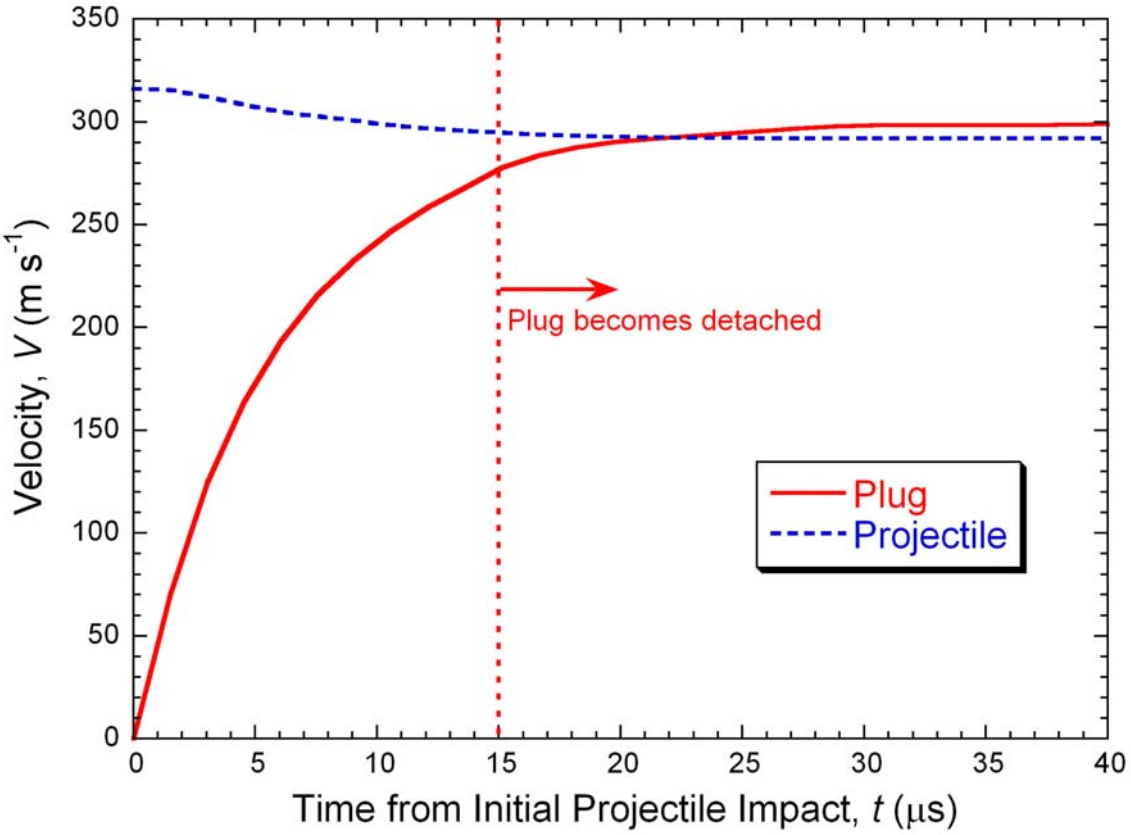
Velocity, V (m s-1)
Time from Initial Projectile Impact, t (μs)
Plug becomes detached
Plug
Projectile
0
50
100
150
200
250
300
350
0
5
10
15
20
25
30
35
40

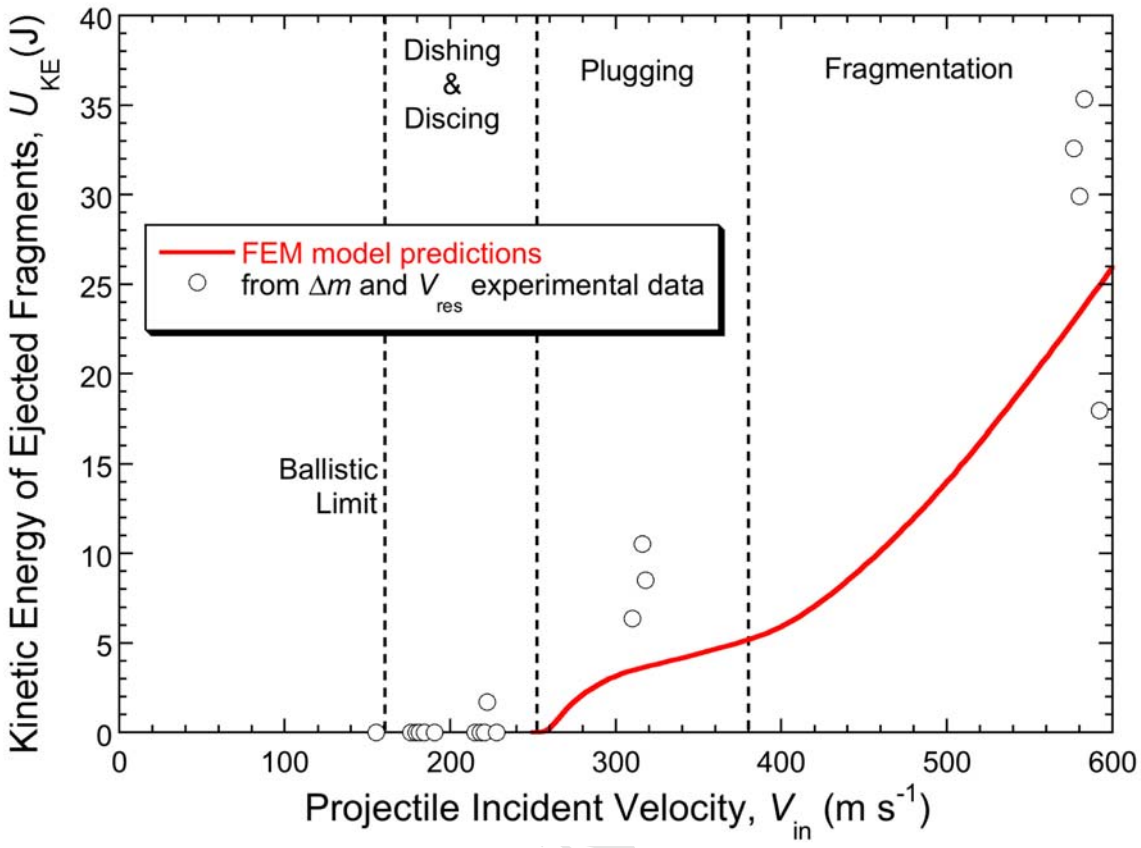
Kinetic Energy of Ejected Fragments, U_{KE} (J)
Projectile Incident Velocity, V_{in} (m s^{-1})
Dishing & Discing
Plugging
Fragmentation
Ballistic Limit
FEM model predictions
from Δm and V_{res} experimental data
0
5
10
15
20
25
30
35
40
0
100
200
300
400
500
600

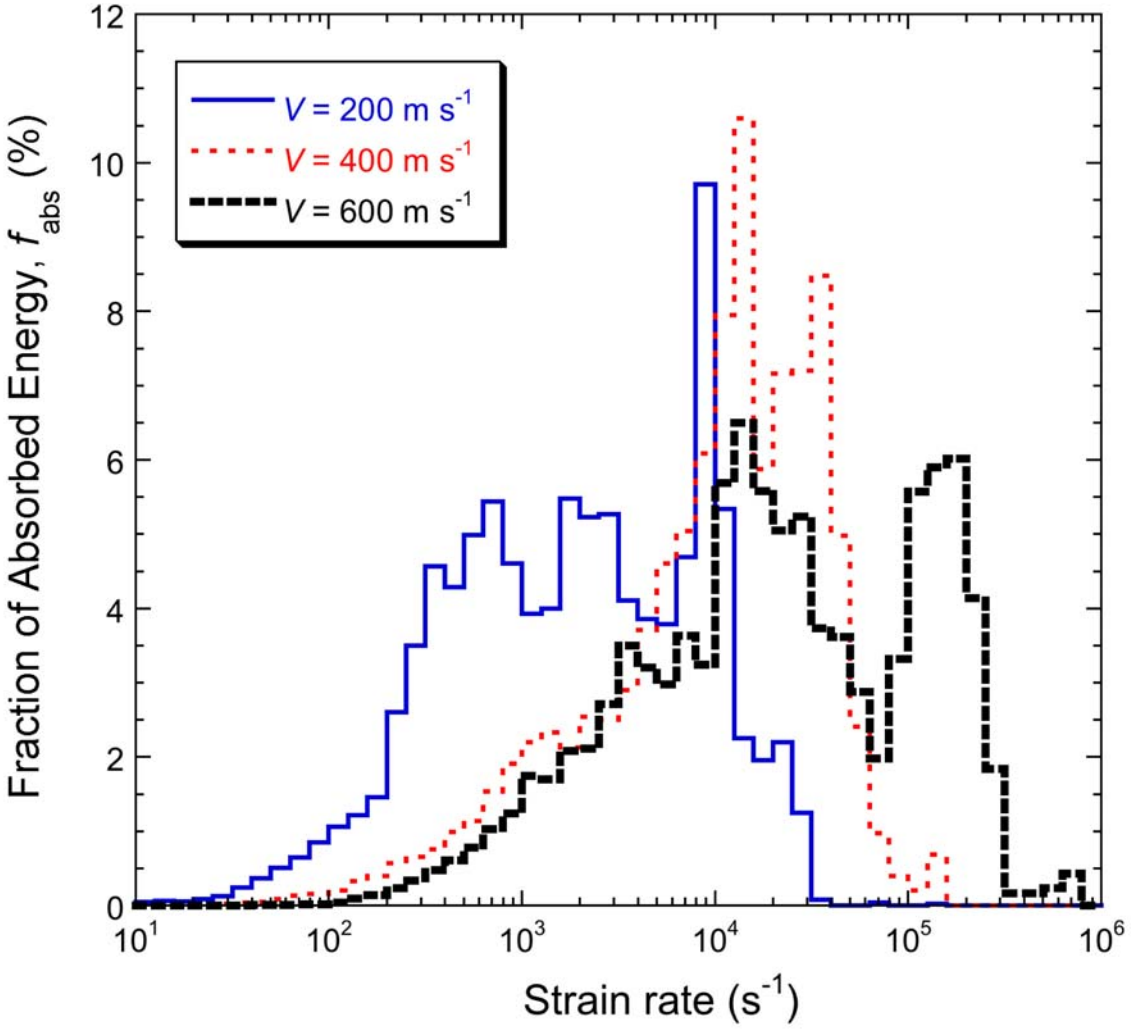
V = 200 m s-1
V = 400 m s-1
V = 600 m s-1
Fraction of Absorbed Energy, f abs (%)
Strain rate (s-1)
0
2
4
6
8
10
12
10^1
10^2
10^3
10^4
10^5
10^6

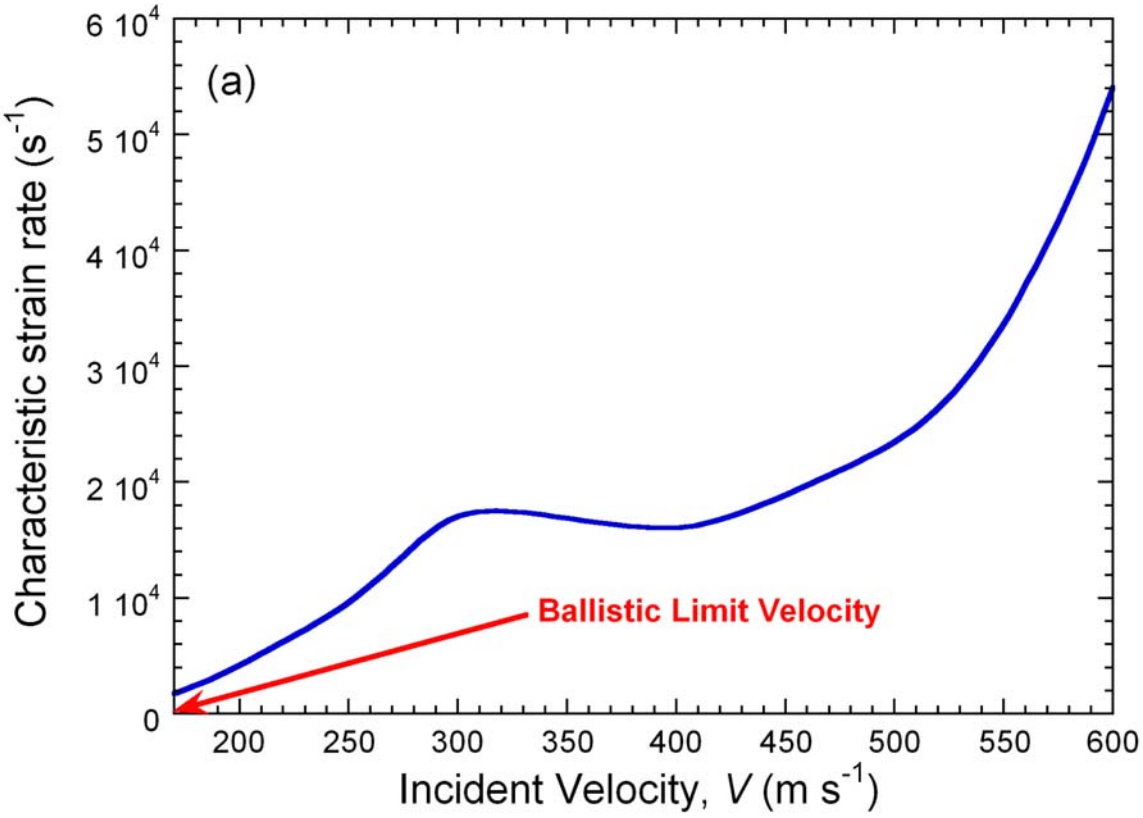
(a)
Characteristic strain rate (s^{-1})
6 10^4
5 10^4
4 10^4
3 10^4
2 10^4
1 10^4
0
200
250
300
350
400
450
500
550
600
Incident Velocity, V (m s^{-1})
Ballistic Limit Velocity

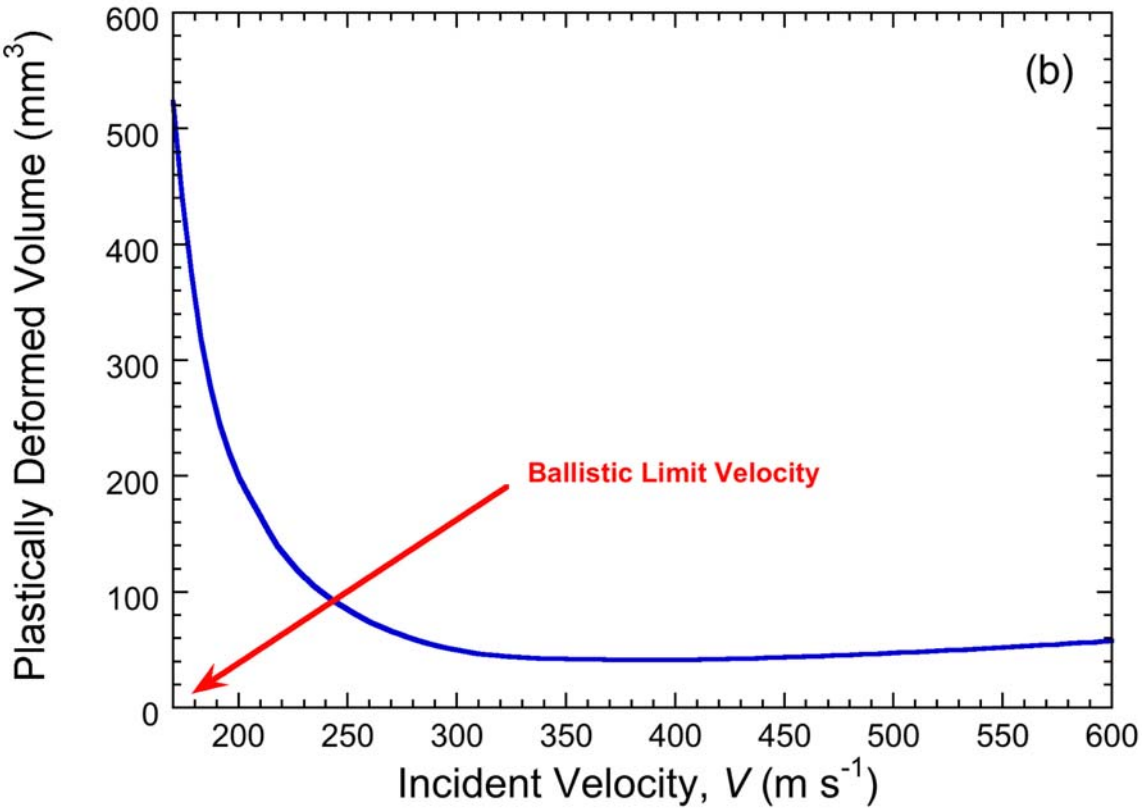
(b)
Plastically Deformed Volume (mm^3)
Incident Velocity, V (m s^{-1})
Ballistic Limit Velocity
0
100
200
300
400
500
600
200
250
300
350
400
450
500
550
600